Supplement of Weather Clim. Dynam., 6, 1443–1459, 2025 https://doi.org/10.5194/wcd-6-1443-2025-supplement © Author(s) 2025. CC BY 4.0 License.





Supplement of

Seasonal Predictability of Vapor Pressure Deficit in the western United States

Melissa L. Breeden et al.

Correspondence to: Melissa L. Breeden (melissa.breeden@noaa.gov)

The copyright of individual parts of the supplement might differ from the article licence.

S1. LIM Tests

 Penland and Sardeshmukh (1995) outline a series of tests to ensure the LIM that has been constructed behaves according to the underlying assumptions of a linear system forced by white noise. The noise covariance matrix should be positive and less than one, as is the case in both LIMs constructed here (Table S1), confirming the system composed by the state vector may be approximated by the LIM components, namely the deterministic operator and the noise. Another test is the behavior of the error; the error of both LIMs used in this study closely matches the error predicted from theory and is lower that of forecasts from persistence and a first-order autoregressive process (Fig. S3).

In a perfectly linear system, the LIM would be independent of its training lag τ_o , while in reality this is not the case due to imperfect observations and nonlinearities (discussed further in Penland and Sardeshmukh 1995). One assessment of how linear a system represented by a LIM is, is to test how well the LIM, trained on a lag τ_o can reproduce the lagged covariance at lags longer than τ_o (Newman et al. 2011; example of LIM-predicted covariance for a 12-month lag: $C(12)=G(3)^4*C0)$). For VPD, the observed lagged covariance decreases markedly at a lead time of 6 months and longer, but persists even out to a 36-month lag in the western US (Fig. S4). The lagged covariance expected from the 3-month G produces a very similar evolution, although the amplitude of the covariance is lower than observations. However, this is the case even for the equal-time covariance C0-LIM, implying the variance truncation of VPD also affects the lagged covariance which is not surprising. Nonetheless, overall the evolution and pattern produced by the LIM is generally in good agreement with observations even lags that are 12 times longer than the 3-month training lag, so we conclude the LIM approximation of linearity holds suitably well. This is bolstered by the high forecast skill the LIM is able to produce at longer lead times (Figs. 2-3).

S2. LIM Trend Removal

The least damped eigenmode of the LIM that includes the trend displays a temporal evolution reflecting the trend (Fig. S5a). However, it is possible that some variability in the least damped eigenmode is a convolution with other modes of the system. For these reasons, the Gram-Schmidt orthogonalization procedure (Lankham et al. 2024) is used to remove any projection of other modes onto the least damped eigenmode, resulting in a time series with lower variability and behavior more indicative of the long-term warming trend (Fig. S5b). The pattern associated with this modified time series is determined by regressing the time series onto the VPD/SST/SM components of the state vector, and the combination of the time series and pattern are used to create trend-related anomalies for each timestep and variable in the record. To detrend each variable, these trend-related anomalies are subtracted from the full field anomalies. A new LIM is constructed using the detrended VPD and SST anomalies as described in the Methods section. Time series of area-averaged VPD and SSTs with and without the trend thus defined confirm that this method of detrending has the desired effect (Fig. S6).

LIM with Trend:	LIM without Trend:
$eig(\mathbf{Q})$	$eig(\mathbf{Q})$
0.0008	0.0023
0.0017	0.0029

0.0033	0.0032
0.0037	0.0040
0.0041	0.0042
0.0044	0.0050
0.0051	0.0055
0.0060	0.0068
0.0069	0.0073
0.0077	0.0085
0.0093	0.0090
0.0103	0.0096
0.0130	0.0111
0.0136	0.0133
0.0181	0.0147
0.0219	0.0166
0.0246	0.0174
0.0315	0.0198
0.0499	0.0232
0.0663	0.0267
0.0975	0.0422
0.1333	0.0556
0.1848	0.1179
	0.1234
	0.1885

Table S1: Eigenvalues of the noise parameters of the LIM including the trend (left column) and the LIM without the trend (right column) for each mode: there are 23 and 25 modes for the LIM including and removing the trend, respectively.

S3. Supplemental Figures

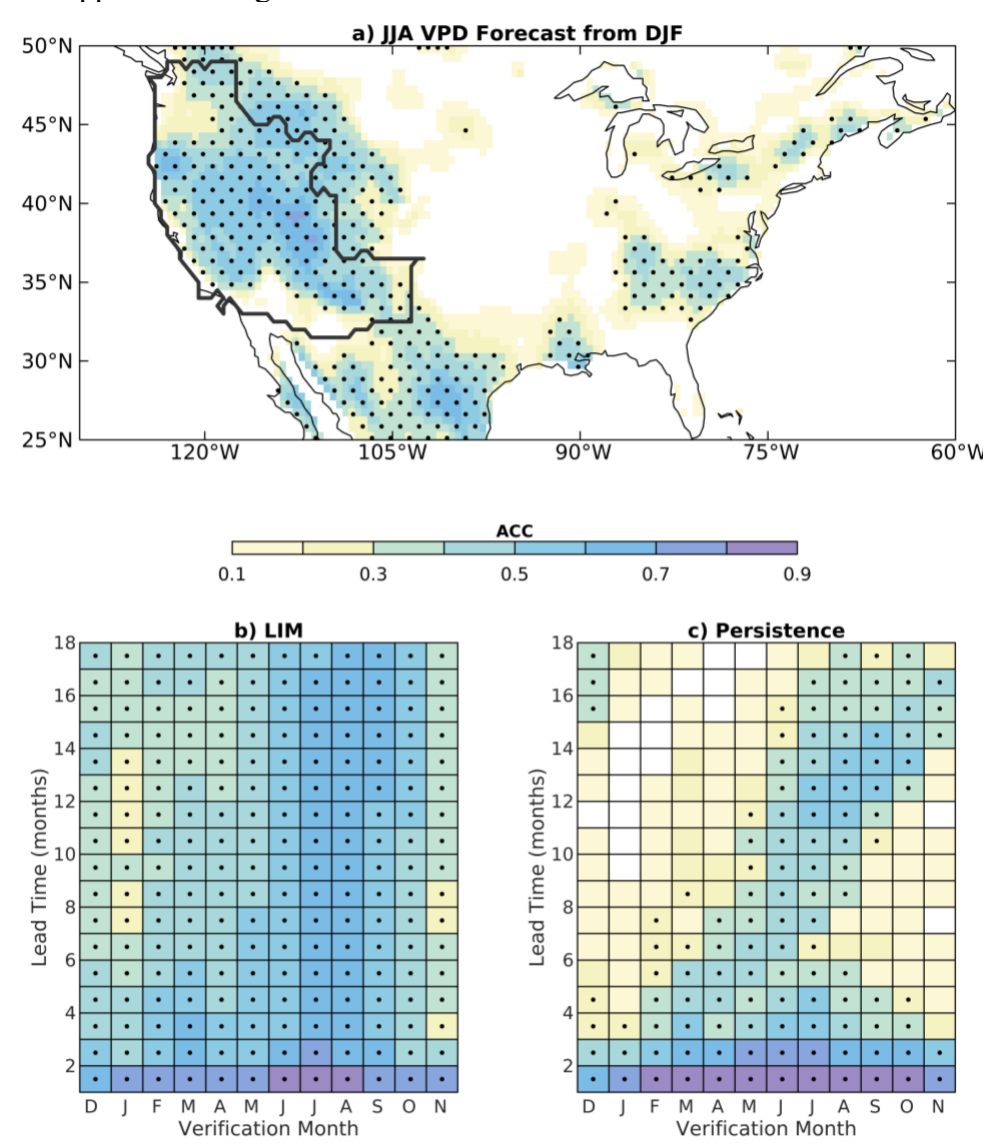


Fig. S1: As in Figure 2 but using a LIM trained with NOAA Extended Reconstructed SST V5 (ERSSTv5; Huang et al. 2017) anomalies instead of JRA-55 SST anomalies. Note: panel c) is identical to Fig. 2c.

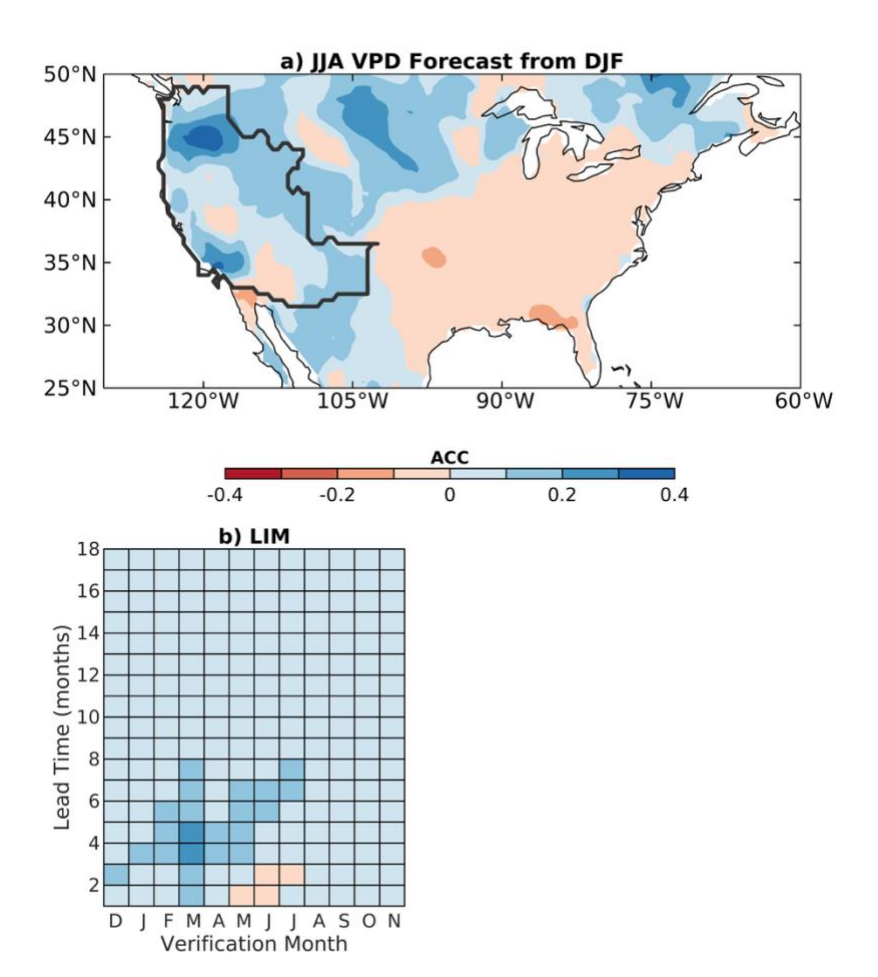


Fig. S2. ACC difference between the LIM including SM subtracted from the LIM without SM (SM - no SM). Positive (blue) values indicate skill improvements with the inclusion of SM.

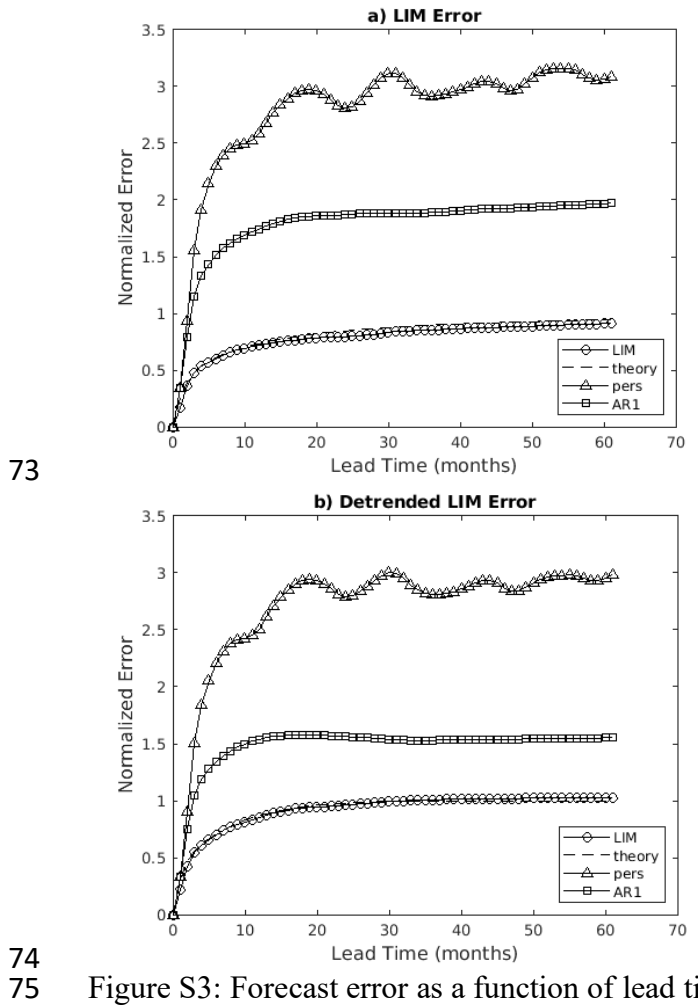


Figure S3: Forecast error as a function of lead time for the LIM compared to error from persistence and AR(1) forecasts, as well as the LIM error that is expected from theory, trace(E), for a) the LIM including the trend and b) the LIM without the trend.

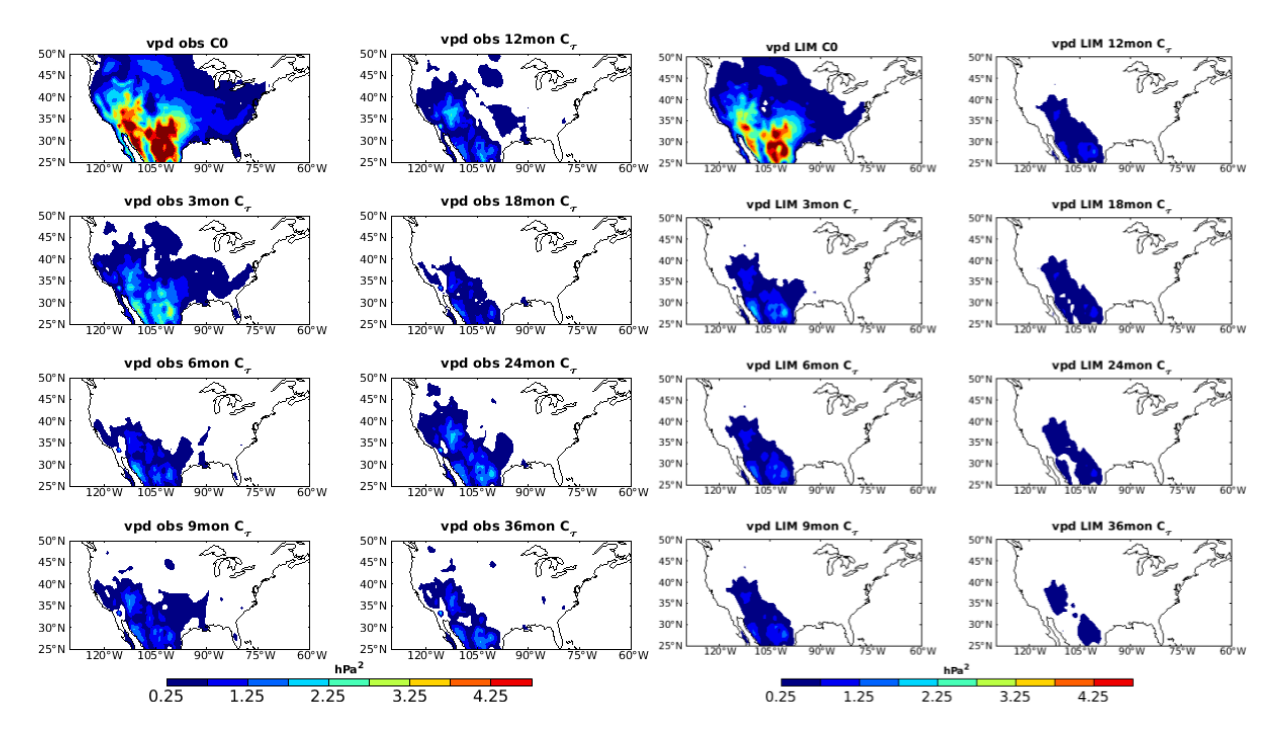


Figure S4: Observed (left two columns) and LIM-calculated (right two columns) VPD covariance calculated at lags from 0 - 36 months.

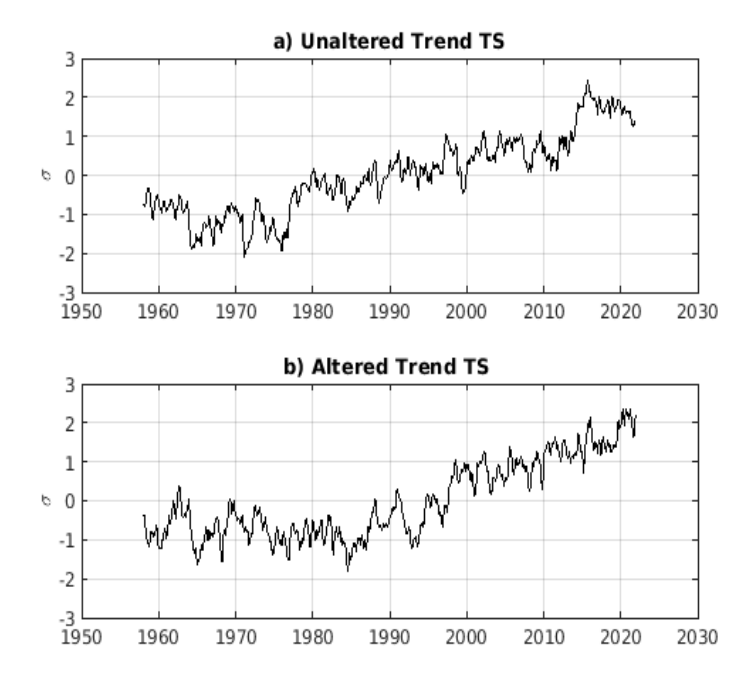


Figure S5: a) Time series of the unaltered least damped LIM eigenmode and b) the modified 'trend' time series after the Gram-Schmidt orthogonalization procedure has been performed.

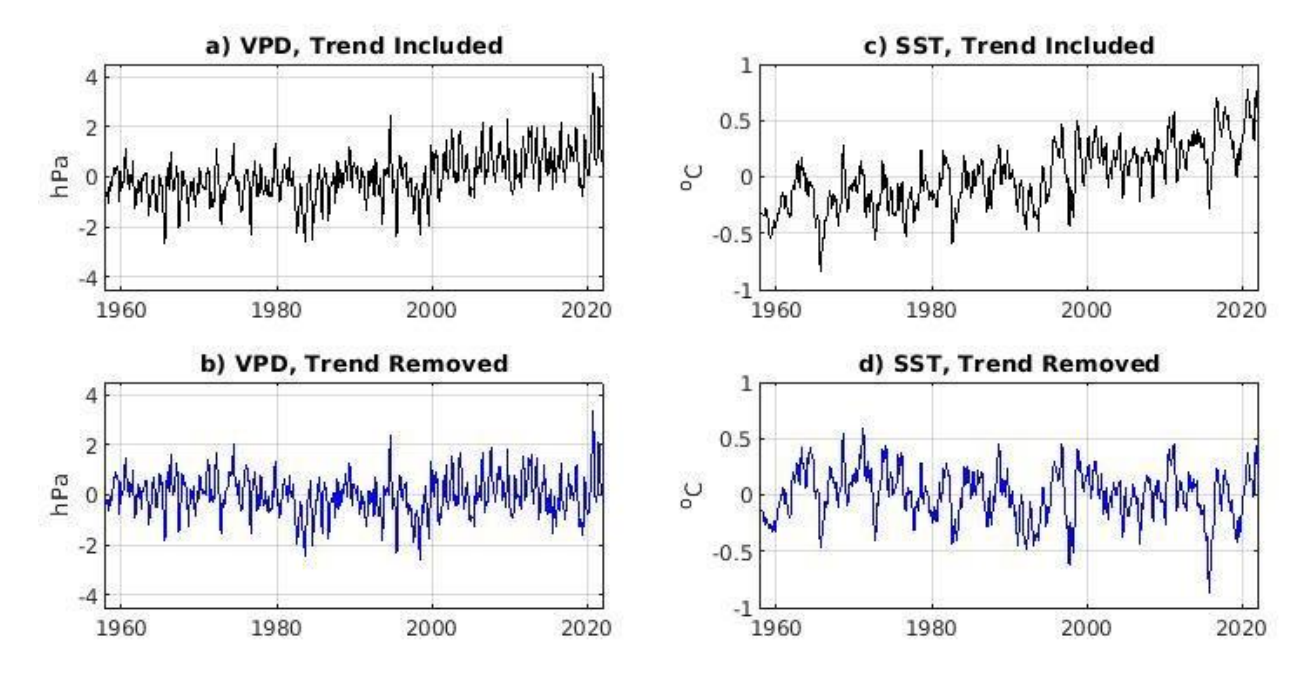


Figure S6: Panels a) – b) show the time series of VPD anomalies averaged over the western US GACCs (Fig. 1), computed a) before and b) after the trend is removed. Panels c) – d) show the time series of SST anomalies averaged over the western tropical Pacific (5° S - 10° N, $120 - 160^{\circ}$ E) computed a) before and b) after the trend is removed.

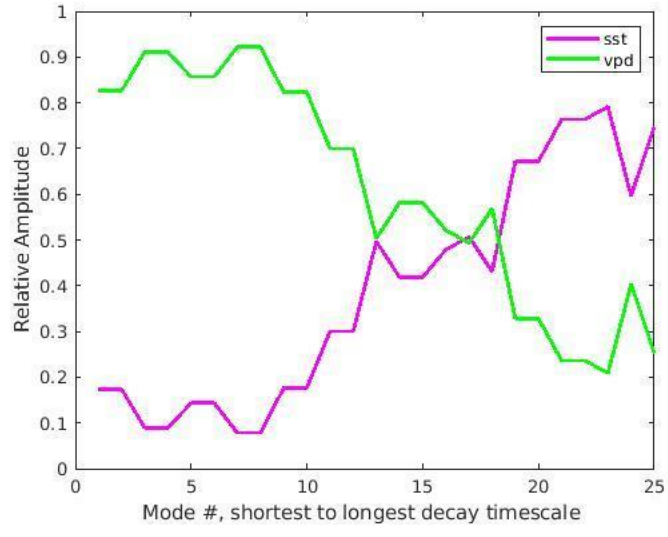


Figure S7: Relative amplitude of each mode in the detrended LIM. Modes are arranged from shortest (left) to longest (right) e-folding timescale.

Mode #	Period (months)	E-folding Timescale
1,2	60.1940	(months) 1.5369

3,4	12.3509	1.5439
5,6	537.2377	2.0707
7,8	20.1352	2.2749
9,10	16.0148	2.5968
11,12	40.7331	2.7562
13	0	3.6566
14,15	37.0622	4.1187
16	0	4.6003
17	0	5.7027
18	0	7.0340
19,20	30.3200	8.0506
21,22	83.1904	9.5954
23	0	11.5343
24	0	17.0438
25	0	19.0051

Table S2: E-folding timescale and period of detrended LIM eigenmodes. Modes 1-10 (red) represent the VPD-only subspace while Modes 11-15 (blue) compose the SST-VPD subspace.

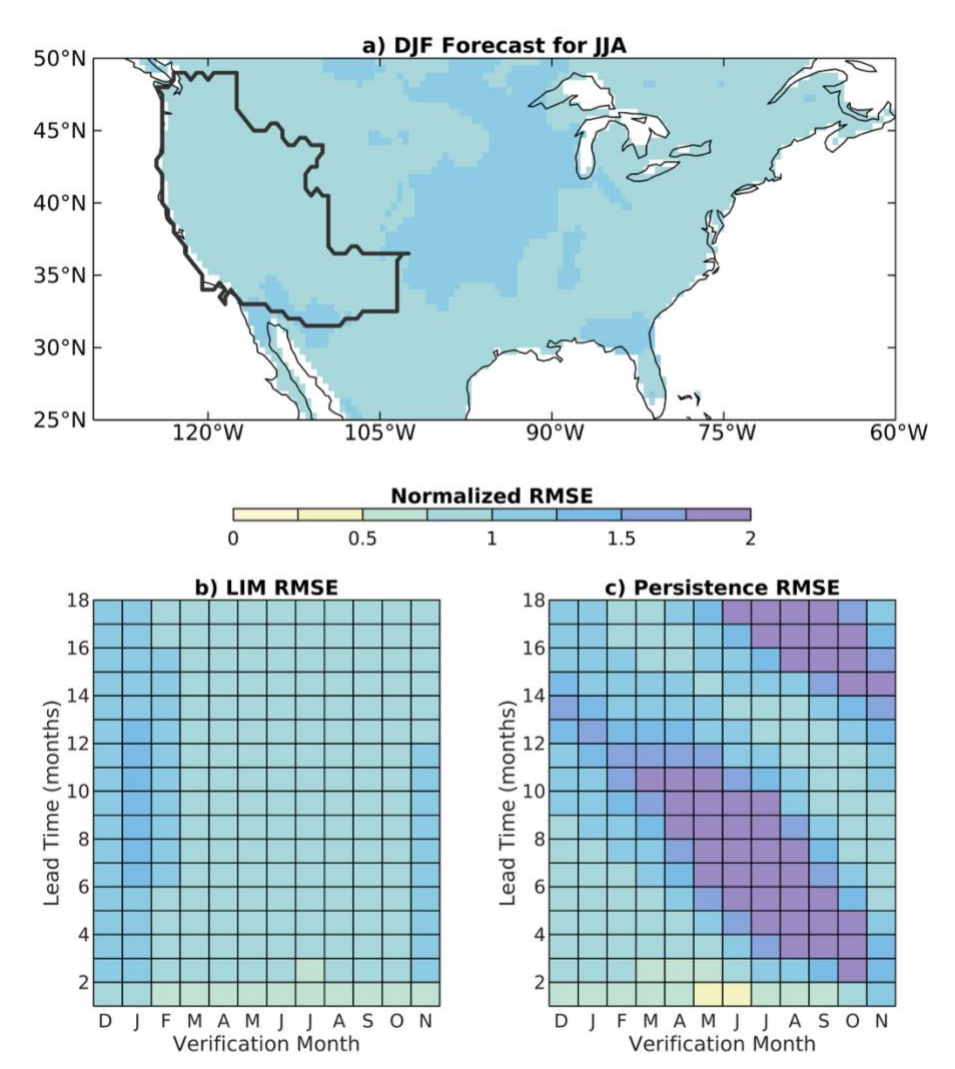


Fig. S8: As in Figure 2 but for root-mean-square error (RMSE) of VPD. Panel a) RMSE of DJF LIM forecasts made for the following JJA, b) area-averaged LIM forecasts and c) a persistence forecast. RMSE is normalized by the standard deviation of the observed VPD anomalies, which is calculated for each verification month separately.

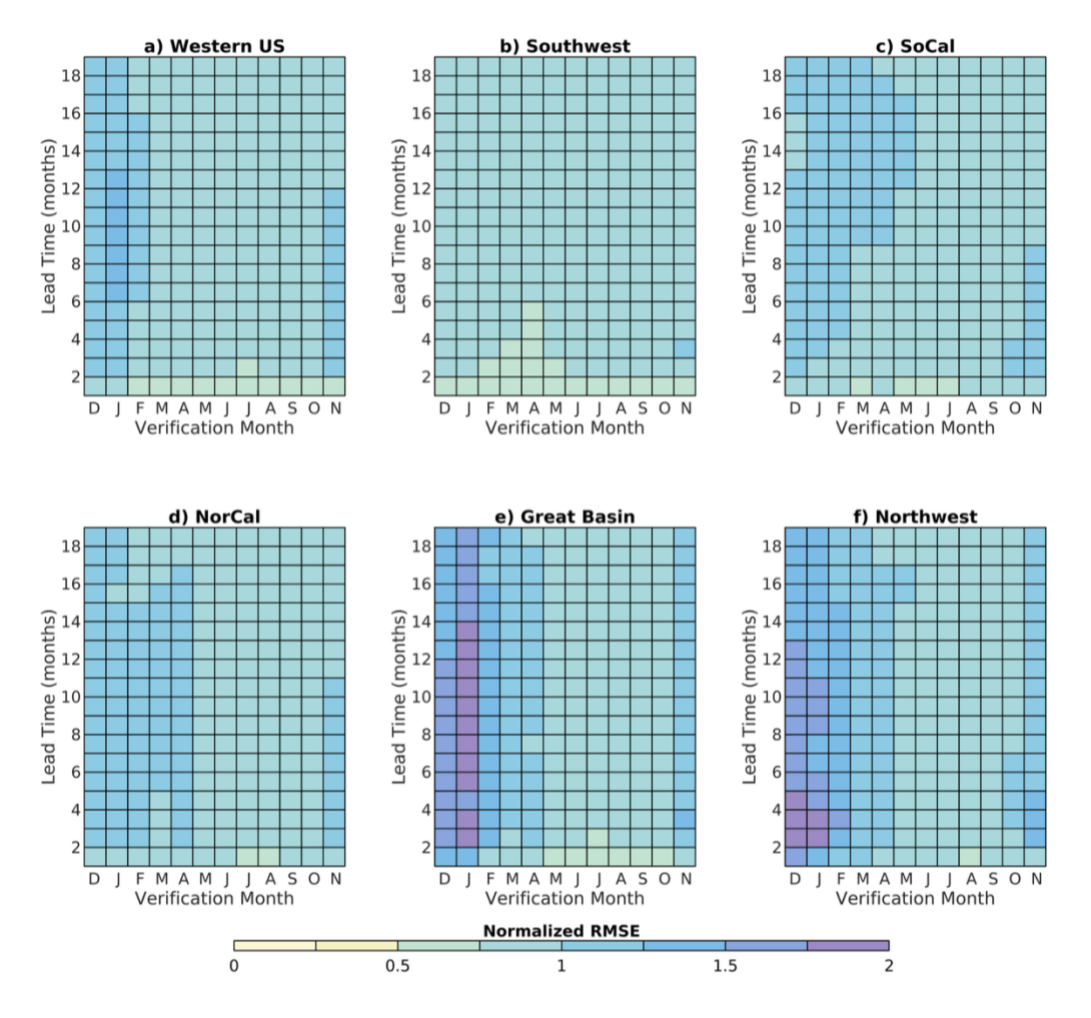


Fig. S9: Normalized RMSE averaged over a) the western US (Fig. 2a), b) Southwest, c) Southern California (SoCal), d) Northern California (NorCal), e) Great Basin, and f) Northwest subregions for LIM forecasts that included the trend in its suite of unfiltered ICs.

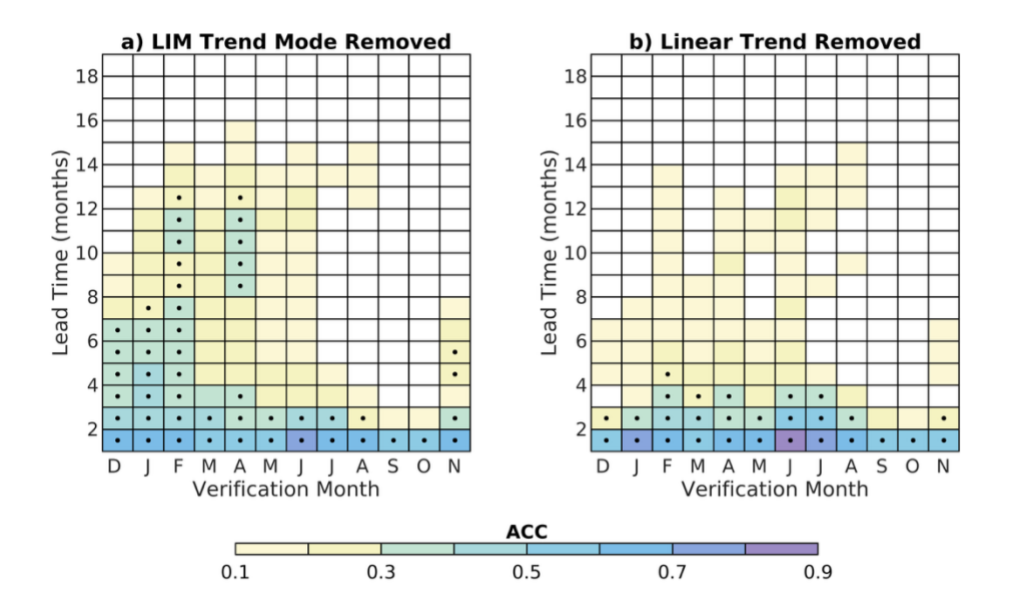


Figure S10: Area-averaged (see Fig. 1) ACC of VPD in the detrended LIM, using a) full initial conditions (ICs) and LIM-based least damped eigenmode method of trend removal, b) full ICs and linear detrending method of trend removal. Both forecasts are verified against detrended VPD anomalies using the altered least damped eigenmode.

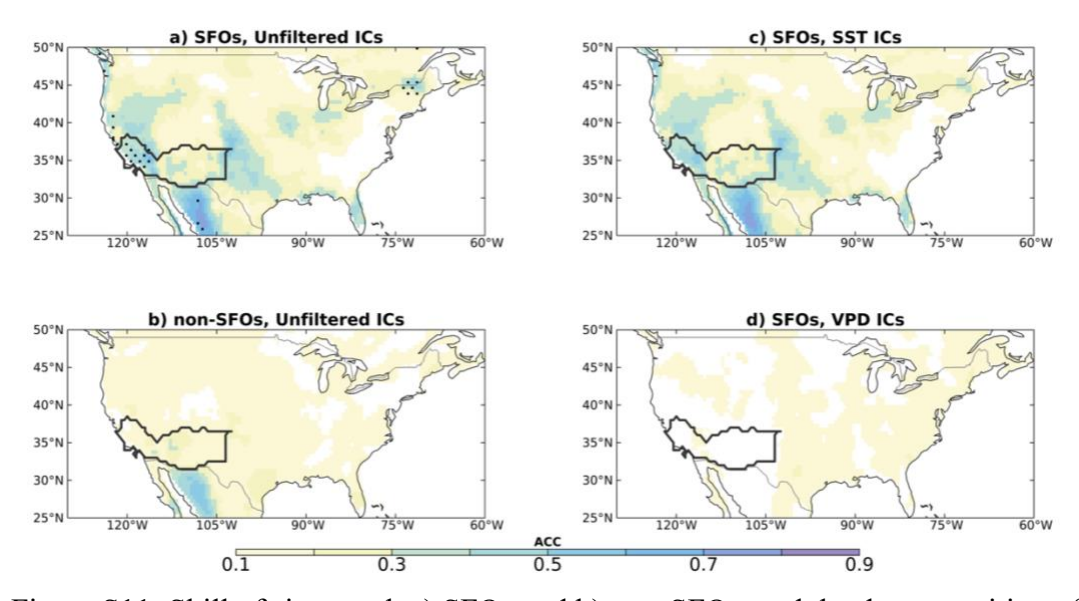


Figure S11: Skill of six-month a) SFOs and b) non-SFOs, and the decomposition of SFO skill into c) SST-VPD and d) VPD-only contributions. Black stippling in panel a) shows where SFO ACC is statistically significantly different from non-SFO ACC at 95% confidence.

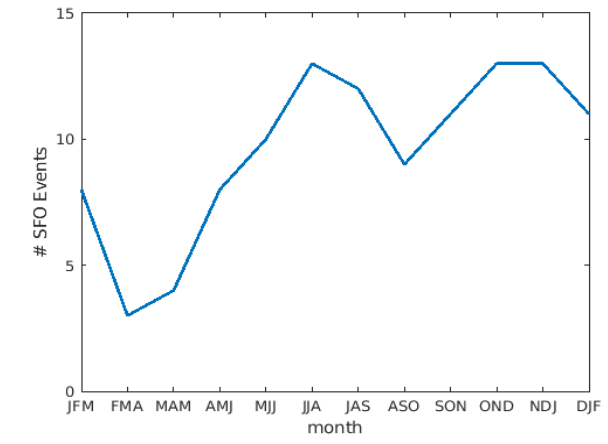


Figure S12: Number of three-month lead time SFOs counted for each initialization season.

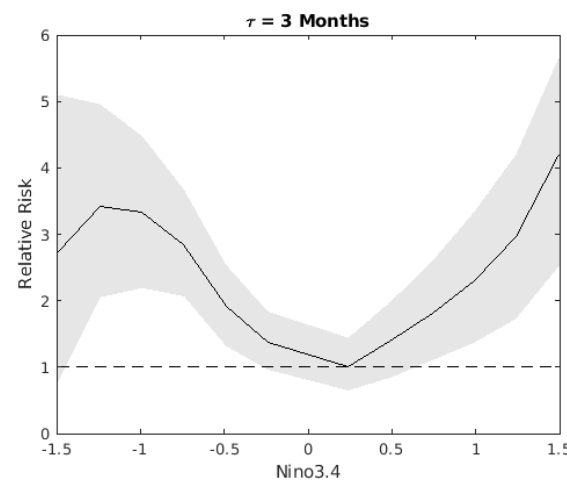


Fig. S13: Relative risk of 3-month lead time VPD SFOs as a function of Niño3.4. The risk is relative to the unconditional probability of an SFO occurring, which is 0.15.

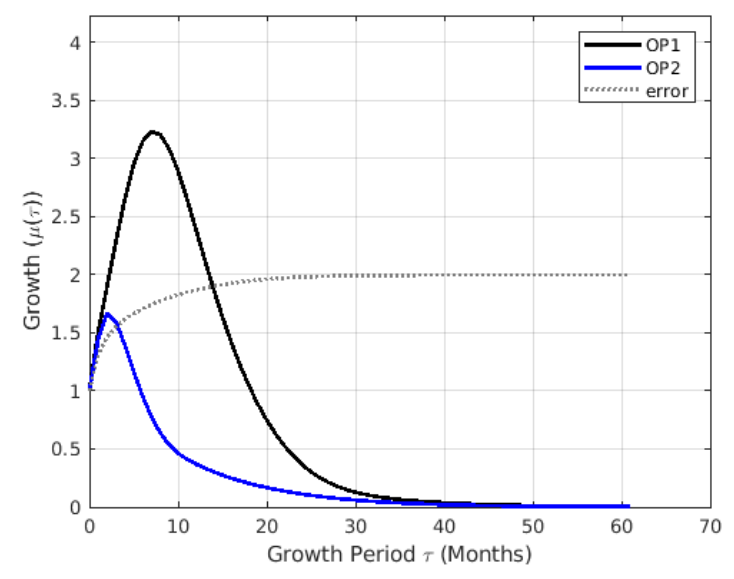


Figure S14: System growth measured by the first (black, OP1) and second (blue OP2) greatest eigenvalues, as a function of growth period, for OP1 and OP2. The black dotted line shows the growth associated with the error covariance, trace(**E**).

References

Huang, B., Peter W. Thorne, Viva F. Banzon, Tim Boyer, Gennady Chepurin, Jay H. Lawrimore, Matthew J. Menne, Thomas M. Smith, Russell S. Vose, and Huai-Min Zhang (2017): NOAA Extended Reconstructed Sea Surface Temperature (ERSST), Version 5. NOAA National Centers for Environmental Information. doi:10.7289/V5T72FNM. Obtain at NOAA/ESRL/PSD at their website https://www.esrl.noaa.gov/psd/ [last accessed May 25, 2025].

Lankam, I. Nachtergaele, B., and Schilling A.: Linear Algebra, LibreTexts, 2024.

Newman, M., Alexander, M., and Scott, J.D.: An empirical model of tropical ocean dynamics. Climate Dynamics, 37(9–10), 1823–1841, 2011.

Penland, C., and Sardeshmukh, P.D.: The optimal growth of tropical sea surface temperature anomalies. Journal of Climate, 8, 1999–2024, 1995.